ROYAL SOCIETY
OF CHEMISTRY

PAPER

Check for updates

An iron-doped NASICON type sodium ion battery cathode for enhanced sodium storage performance and its full cell applications†

Jae Yeol Park, [ID] [a] Yoonsu Shim, [ID] [a] Yong-il Kim, [b] Yuseon Choi, [c] Ho Jun Lee, [a] Jungjae Park, [a] Ji Eun Wang, [ID] [a] Yonghee Lee, [ID] [d] Joon Ha Chang, [ID] [a] Kanghoon Yim, [e] Chi Won Ahn, [d] Chan-Woo Lee, [e] Do Kyung Kim [ID] [a] and Jong Min Yuk [ID] *[a]

The development of high performance and cost-effective electrode materials is the main challenge for the commercialization of sodium ion batteries. Here, we suggest a substantial iron-doped sodium vanadium fluorophosphate and sodium vanadium phosphate composite as a promising cathode. Iron substitution enhances ionic diffusivity and lowers the bandgap, and, thus, improves sodium storage performance. The origin of the enhanced performance is investigated employing *in situ* X-ray diffraction, *ex situ* X-ray photoelectron spectroscopy, density functional theory calculation, and electrochemical characterization. Moreover, we demonstrate its full cell configuration with earth-abundant element-based copper sulfide anodes. The suggested cathode and sodium ion battery full cell exhibits well-balanced sodium storage performance in terms of energy density, C-rate capability, cycling stability, and low cost. The low cost and high performance of the full cell make it an attractive choice for energy storage systems and high power applications to support lithium ion batteries.

[a]*Department of Materials Science & Engineering, Korea Advanced Institute of Science and Technology (KAIST), 291 Daehak-ro, Yuseong-gu, Daejeon, 34141, Republic of Korea. E-mail: jongmin.yuk@kaist.ac.kr*

[b]*Korea Research Institute of Standards and Science, 267 Gajeong-ro, Yuseong-gu, Daejeon, Republic of Korea*

[c]*Department of Chemical Engineering, Konkuk University, 120 Neungdong-ro, Gwangjin-gu, Seoul, Republic of Korea*

[d]*National Nano Fab Center (NNFC), 291 Daehak-ro, Yuseong-gu, Daejeon, 34141, Republic of Korea*

[e]*Platform Technology Laboratory, Korea Institute of Energy Research, 152 Gajeong-ro, Yuseong-gu, Daejeon, 34129, Republic of Korea*

† Electronic supplementary information (ESI) available. See DOI: 10.1039/d0ta07766f

Introduction

Lithium-ion batteries (LIBs) have been employed in various applications such as electronic devices, electric vehicles (EVs), and energy storage systems (ESSs) since their first commercialization in the 1990s. However, the high prices of the raw materials, such as lithium, cobalt and nickel, have caused a necessity for the development of an alternative to LIBs. In such a context, sodium-ion batteries (SIBs) have been suggested owing to their inherent low cost.

To develop a high performance SIB, various promising electrode materials have been explored. For anodes, P, graphite, hard carbon, Sn, Bi, FeS_x, and Cu_xS have been suggested.[1–9] Especially, graphite, Sn, Bi, and Cu_xS show exceptional cycling stability in ether-based electrolytes without material optimization.[5–10] For cathode materials, Na super ion conductor (NASICON) type materials, such as sodium vanadium fluorophosphates ($Na_3V_2(PO_4)_2F_3$ (NVPF) and $Na_3V_2O_2(PO_4)_2F$ (NVOPF)) and sodium vanadium phosphate ($Na_3V_2(PO_4)_3$ (NVP)) have been intensively studied due to their stable cyclability and high discharge voltages (~3.9 V for NVPF, ~3.8 V for NVOPF, and ~3.4 V for NVP).[11–13]

However, the pure NASICON type materials rarely exhibit their theoretical capacity owing to relatively low ionic diffusivity and electronic conductivity.[14–16] Furthermore, the NASICON type materials include a high content of expensive vanadium, which makes them economically less competitive. Therefore, we perform replacement of V in a NVPF/NVP composite with inexpensive transition metals to improve its sodium storage performance and economic competiveness.

We find an optimal substituting element and substitution quantity. Furthermore, we investigate the origin of the performance improvement utilizing *in situ* XRD, *ex situ* XPS, electrochemical characterization, and DFT calculation. Finally, we realize a full-cell configuration of the improved NVPF/NVP composite and bulk CuS as an economically reasonable high performance SIB.

Results and discussion

Structural and electrochemical characterization of Fe-doped NVPF/NVP

Six transition metals, such as Fe, Cr, Mn, Ti, Cu, and Zn, are considered to replace V in the NVPF/NVP composite owing to
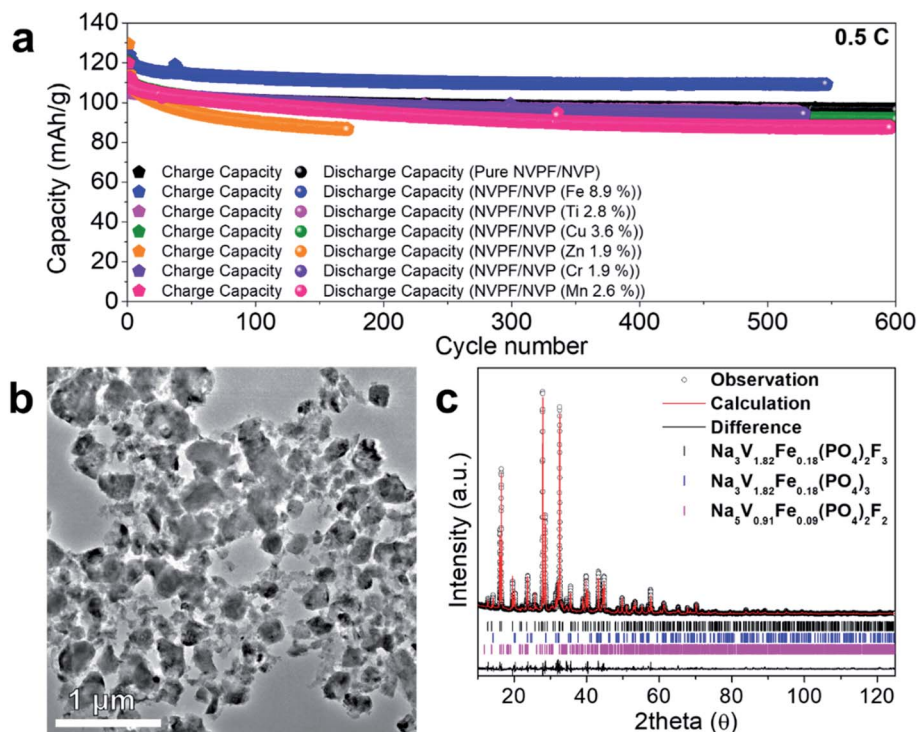
Fig. 1 (a) Cycling performance of undoped NVPF/NVP, and Fe-, Ti-, Cu-, Zn-, Cr-, and Mn-doped NVPF/NVP composites. (b) Low magnification TEM image of NVPF/NVP (Fe 8.9%). (c) Rietveld refinement of NVPF/NVP (Fe 8.9%).

their earth abundances and low costs (Table S1†). The transition metal doped-samples are labelled NVPF/NVP (M x%, M = doped transition metals; x% = content of the transition metals in atomic percent).

Among the candidates, we discover that Fe is the most proper substitutional element to enhance the electrochemical performance, simultaneously with the cost reduction of raw materials.

Fe substitutes 8.9% of V in NVPF/NVP with improved sodium storage capacity, while, in the other transition metal cases, more than 3.6% of substitutions into the material induce performance degradations (Fig. 1a). Here, the contents of the doped elements are obtained by inductively coupled plasma (ICP) analysis. Undoped NVPF/NVP and Fe-doped NVPF/NVP composites are characterized utilizing Rietveld refinement and TEM (Fig. 1b and c, S1 and S2†). The Rietveld analysis confirms the co-existence of two major phases, NVPF and NVP phases. With an Fe content of 4.9%, the two phases exist in the composite. With more Fe content, a minor phase of

$Na_5V_{0.91}Fe_{0.09}(PO_4)_2F_2$ appears, which is isostructural with previously reported $Li_5V(PO_4)_2F_2$.[17] The detailed lattice parameters and crystal structures are presented in Table 1 and Fig. S3.†

NVPF/NVP cathodes, substituted with various contents of Fe, are charged and discharged at current densities of 0.5C to 10C (1C = 128 mA h g^{-1}, Fig. 2). All NVPF/NVPs show three main plateaus; (i) the first plateau at ~4.2 V, (ii) second plateau at ~3.7 V, (iii) and third plateau at ~3.4 V (Fig. 2a). Here, undoped NVPF/NVP shows slightly sloping discharge voltage plateaus compared to Fe-doped NVPF/NVPs (Fe 4.9%, 8.9%). It implies that the NVPF phase in undoped NVPF/NVP is partially oxidized.[18]

With an Fe content of 4.9%, the average discharge voltage remains well above 3.7 V at 0.5C (Fig. 2b). However, upon further increase of the Fe content to over 4.9%, the average discharge voltage starts to decrease due to the reduced $Na_3V_{2-x}Fe_x(PO_4)_2F_3$ amount (Fig. S4†), which lowers a portion of the first (~4.2 V) and second (~3.7 V) plateaus. In addition,

Table 1 Lattice parameters of the phases in NVPF/NVP (Fe 0%, 4.9%, and 8.9%)

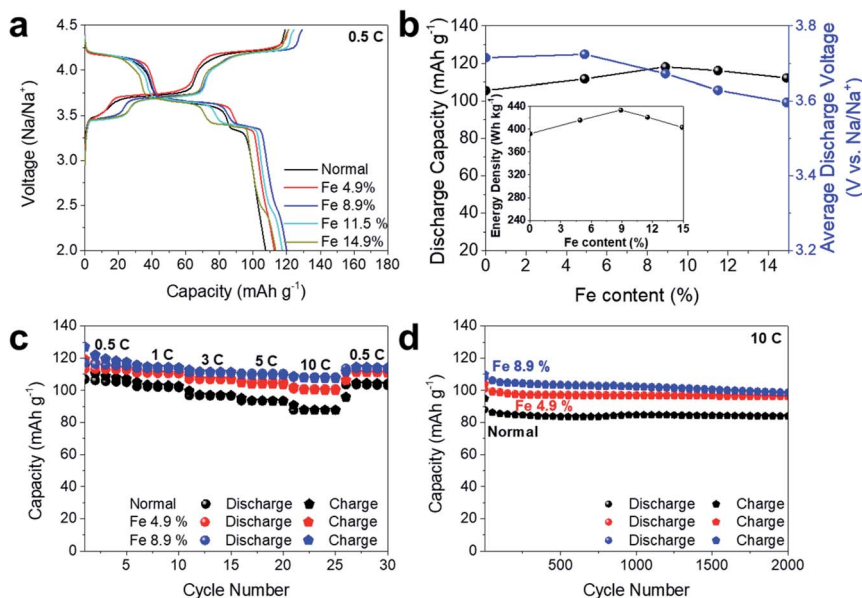| Phases	Fe content (%)	a (Å)	b (Å)	c (Å)	Vol. (Å^3)
$Na_3V_{2-x}Fe_x(PO_4)_2F_3$	0	9.03490	9.03490	10.74650	877.23789
	4.9	9.03550	9.03550	10.74690	877.37971
	8.9	9.03998	9.03998	10.73190	877.02416
$Na_3V_{2-x}Fe_x(PO_4)_3$	0	8.72236	8.72236	21.93000	722.44915
	4.9	8.74100	8.74100	21.80800	721.50395
	8.9	8.73780	8.73780	21.73200	718.46321

Fig. 2 Electrochemical performance of NVPF/NVP (Fe 0–14.9%). (a) Charge and discharge profiles of NVPF/NVPs (Fe 0–14.9%) at 0.5C. (b) Discharge capacity, average discharge voltage, and energy density changes of Fe-doped NVPF/NVP as a function of Fe content. (c) C-rate capability and (d) cycling stability of NVPF/NVP (Fe 0%, 4.9%, 8.9%). The values in (b) are on the basis of the 5th cycle at 0.5C.

a clear new plateau appears at ∼2.5 V from an Fe content of 8.9%, which is induced by the Fe-doped NVP phase.[19] Nevertheless, Fe-doped NVPF/NVP reaches the best Na storage performance at an Fe content of 8.9%. Although NVPF/NVP (Fe 8.9%) has a slightly lowered average discharge voltage of ∼3.67 V, it has the highest capacity of ∼118 mA h g^{-1} to deliver the highest energy density of ∼433 W h kg^{-1} (5th cycle, 0.5C, Fig. 2b).

Considering the highest energy density, the Fe content of 8.9% is the most optimal amount. With Fe contents of 11.5% and 14.9%, they show energy densities of 421 W h kg^{-1} and 403 W h kg^{-1}, still higher than before undoped NVPF/NVP.

Table 2 Performance comparison between NVPF/NVP (Fe 8.9%) and recently reported NVPF/NVP, NVPF, and NVOPF. Average voltages of the materials are obtained using a web-based data extraction tool in https://apps.automeris.io/wpd/

Materials	Capacity @ 0.5C (mA h g^{-1})	Average discharge voltage @ 0.5C (V)	C-rate capability	Capacity retention	Reference
NVPF/NVP (Ti 5%)	122.96 (1st cycle)	3.66	112 mA h g^{-1} @ 10C 107 mA h g^{-1} @ 20C 102.5 mA h g^{-1} @ 40C	91 mA h g^{-1} @ 1C after 200 cycles (∼77%)	14
NVPF/NVP (Y 2.5%)	122.26 (1st cycle)	3.6	106 mA h g^{-1} @ 5C 87 mA h g^{-1} @ 10C	115 mA h g^{-1} @ 1C after 200 cycles (∼93%)	15
NVPF (Mn 2.5%)	122.87 (1st cycle)	3.74	79 mA h g^{-1} @ 5C 60 mA h g^{-1} @ 10C	109 mA h g^{-1} @ 1C after 500 cycles (∼91%)	16
Ru-doped NVOPF	116.4 (1st cycle)	3.49	107.8 mA h g^{-1} @ 10C 101.8 mA h g^{-1} @ 20C 75 mA h g^{-1} @ 60C	83 mA h g^{-1} @ 20C after 2000 cycles (∼81%)	20
NVPF@rGO	122.69 (3rd cycle)	3.68	115 mA h g^{-1} @ 10C 106.8 mA h g^{-1} @ 20C	84 mA h g^{-1} @ 20C after 2000 cycles (∼78%)	21
NVOPF nanocuboid array	130 (1st cycle)	3.6	102 mA h g^{-1} @ 8C 96.6 mA h g^{-1} @ 15C 59.5 mA h g^{-1} @ 50C	55.6 mA h g^{-1} @ 20C after 2000 cycles (∼88%)	22
NVOPF array@carbon fiber	119.2 (1st cycle)	3.63	79.5 mA h g^{-1} @ 5C 65.5 mA h g^{-1} @ 20C	65.5 mA h g^{-1} @ 5C after 500 cycles (∼82%)	23
NVPF/NVP (Fe 8.9%)	**119.88 (1st cycle)**	**3.64**	**110 mA h g^{-1} @ 5C** **108 mA h g^{-1} @ 10C**	**109.2 mA h g^{-1} @ 0.5C after 500 cycles (∼91%)** **102.8 mA h g^{-1} @ 10C after 1000 cycles (∼95%)** **98.5 mA h g^{-1} @ 10C after 2000 cycles (∼91%)**	**This work**

20438 | J. Mater. Chem. A, 2020, **8**, 20436–20445

This journal is © The Royal Society of Chemistry 2020

Fe substitution also enhances the C-rate capability of the cathode (Fig. 2c). After 2000 cycles at 10C, NVPF/NVP (Fe 8.9%), NVPF/NVPF (Fe 4.9%), and undoped NVPF/NVP retain 98.5 mA h g^{-1}, 97 mA h g^{-1}, and 87 mA h g^{-1}, respectively (Fig. 2d).

NVPF/NVP (8.9%) exhibits well-balanced performance in terms of capacity, average discharge voltage, C-rate capability, and capacity retention, and thus is highly competitive to previously reported NVPFs and NVOPFs. To assess the performance of NVPF/NVP (Fe 8.9%), it is compared to recently reported similar cathodes[14–16,20–23] (Table 2). Ti and Y doped NVPF/NVP and Mn-doped NVPF exhibit high capacities of ~122 mA h g^{-1}. However, Ti-doped NVPF shows a relatively poor capacity retention rate of ~77% at 1C after just 200 cycles. For Y-doped and Mn-doped NVPFs, although they present high cycling stabilities at 1C, they exhibit relatively poor C-rate capabilities

with 87 mA h g^{-1} at 10C and 60 mA h g^{-1} at 10C. Furthermore, doping amounts of Ti, Y, and Mn are limited to 5%, 2.5%, and 2.5%, respectively. Ru-doped NVOPF shows a relatively low average discharge voltage.

NVPF/NVP (Fe 8.9%) is also highly competitive to recently reported NVPF and NVOPFs with a specific morphology or combined with rGO or other carbon materials.[21–23] NVPF/NVP (Fe 8.9%) exhibits a superior capacity retention of over 90% after 2000 cycles at a high current density of 10C. Although the C-rate capability of NVPF/NVP (Fe 8.9%) is slightly lower than that of the optimized NVPF/rGO composite, considering the higher capacity retention and raw cost reduction with 8.9% Fe, it is one of the most well-optimized V-based NASICON cathodes.

The electrochemical performance improvement in Fe-doped NVPF/NVPs should be related to crystallographic phase
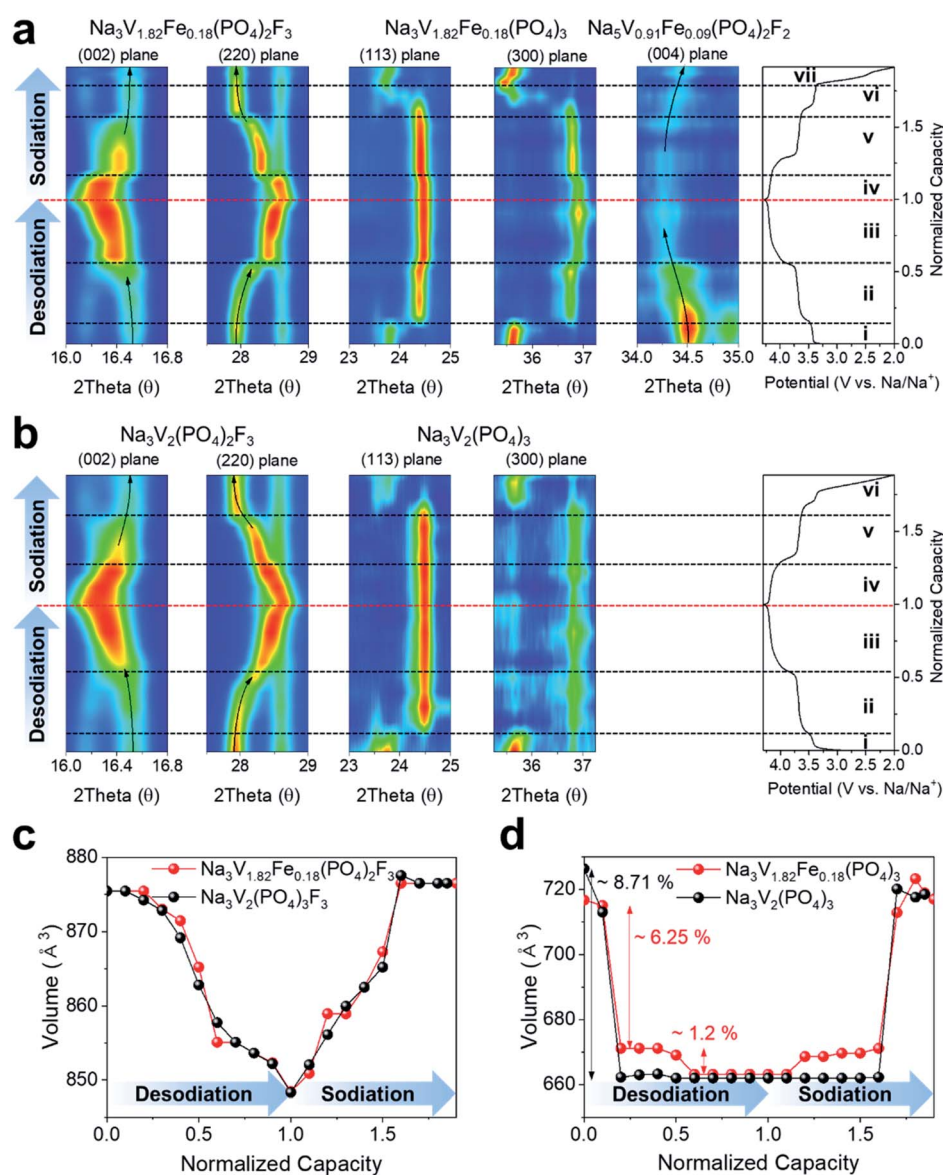

Fig. 3 Crystal structural evolution during desodiation and sodiation. *In situ* X-ray diffraction pattern changes of (a) NVPF/NVP (Fe 8.9%) and (b) normal NVPF/NVP. Unit cell volume variations of (c) undoped NVPF and Fe-doped NVPF in NVPF/NVP (Fe 8.9%) and (d) undoped NVP and Fe-doped NVP in NVPF/NVP (Fe 8.9%).

This journal is © The Royal Society of Chemistry 2020

J. Mater. Chem. A, 2020, 8, 20436–20445 | 20439

evolution during sodiation, valence changes of the transition metals, Na diffusivity, and electronic conductivity. Therefore, we investigate those factors employing *in situ* XRD, *ex situ* XPS, electrochemical characterization, and density functional theory (DFT).

Crystal structural changes in Fe-doped NVPF/NVP during operation

The enhanced performance of Fe-doped NVPF/NVP can be related to the crystal structural evolution and the corresponding volume change in the Na migration path, which affects the migration barrier.[24] The migration tunnel volume should be related to the volumes of the unit cells. In order to investigate crystal structural evolutions during the cell operations, *in situ* transmission X-ray diffraction (XRD) is utilized and correlated with the charge and discharge profiles (Fig. 3).

In NVPF/NVP (Fe 8.9%), unlike undoped NVPF, a and c axes relatively discretely change upon phase transitions of $Na_2V_{1.82}Fe_{0.18}(PO_4)_2F_3 \rightarrow Na_3V_{1.82}Fe_{0.18}(PO_4)_2F_3$ (iv → v) and $Na_2V_{1.82}Fe_{0.18}(PO_4)_2F_3 \leftrightarrow NaV_{1.82}Fe_{0.18}(PO_4)_2F_3$ (ii → iii and iv → v) (Fig. 3, S5 and S6†)[25] indicating the tendency of biphasic reactions. However, it presents a similar volume variation to undoped NVPF/NVP during the operation. Thus, considering the Na migration through a rectangular shape tunnel consisting of 4O atoms (Fig. S7a†),[26] we believe that it would induce a negligible migration barrier change. On the other hand, clearly distinctive crystallographic behaviour is observed in $Na_3V_{1.82}Fe_{0.18}(PO_4)_3$. The Fe-doped NVP experiences a two-step phase evolution during the operation, while undoped NVP experiences a direct one step phase transition of $Na_3V_2(PO_4)_3 \leftrightarrow NaV_2(PO_4)_3$. The Fe-doped NVP experiences phase transitions of $Na_3V_{1.82}Fe_{0.18}(PO_4)_3 \leftrightarrow Na_{1+\alpha}V_{1.82}Fe_{0.18}(PO_4)_3$ and $Na_{1+\alpha}V_{1.82}Fe_{0.18}(PO_4)_3 \leftrightarrow NaV_{1.82}Fe_{0.18}(PO_4)_3$ at ~3.4 V and ~3.9 V in desodiation and at ~3.4 V and ~4.1 V in sodiation. It indicates that Fe-doped NVP contributes to a capacity above 3.4 V, which is quite distinguishable in that undoped NVP makes a capacity contribution with a single plateau at ~3.4 V. Furthermore, the intermediate phase of $Na_{1+\alpha}V_{2-x}Fe_x(PO_4)_3$ plays a role as

a buffer phase for efficient stress accommodation by reducing misfit strains upon the phase transitions. It could facilitate Na diffusion compared to the case of the one step reaction. Considering two Na migration paths in NVP (Fig. S7b and c†), the larger average volume would induce a relatively lower Na migration barrier to enhance the Na diffusivity. For the minor phase, $Na_5V_{0.91}Fe_{0.09}(PO_4)_2F_2$, with tracking of the (004) plane, it makes a capacity contribution between 2.0 V and ~3.7 V.

Valence changes of the transition metals in NVPF/NVPs

A partially oxidized state of the NVPF phase is implied in undoped NVPF/NVP with slightly sloping plateaus in the discharge profile. The oxidation of the NVPF phase forms inherent V^{4+}. Thus, *ex situ* XPS analysis is conducted to confirm it and correlate it with the electrochemical performance. As a result, indeed, the co-existence of V^{3+} and V^{4+} is presented in the V2p spectrum in undoped NVPF/NVP (Fig. 4a). As charged to 3.9 V and 4.45 V, the co-existence of V^{3+}, V^{4+}, and V^{5+} is confirmed, which indicates a co-contribution of V^{3+}/V^{4+} and V^{4+}/V^{5+} redox pairs for the two plateaus at ~3.7 V and ~4.2 V. However, in the charged state to 3.9 V, V^{3+} accounts for about a half area of the total spectrum, and, even in the fully charged state, V^{3+} still remains unreacted, which supports the relatively low capacity of undoped NVPF/NVP. On the other hand, NVPF/NVP (Fe 8.9%) shows a highly symmetric V2p spectrum with V^{3+}, which is converted to highly symmetric V^{4+} with complete oxidation of V^{3+} (Fig. 4b). Besides V, Fe^{3+} also contributes to capacity with being oxidized to Fe^{4+} (Fig. S8†).

Kinetic properties change upon Fe substitution into NVPF/NVP

On the basis of the fully evolved V^{3+}/V^{4+} redox pair, NVPF/NVP (Fe 8.9%) shows significantly improved sodium storage performance compared to undoped NVPF/NVP. Unreacted V^{3+} indicates that $1 + \alpha$ Na still remains in the crystal structure instead of 1 Na, which could hinder sodium migration due to a higher Na defect formation energy.[27] Therefore, we expect higher
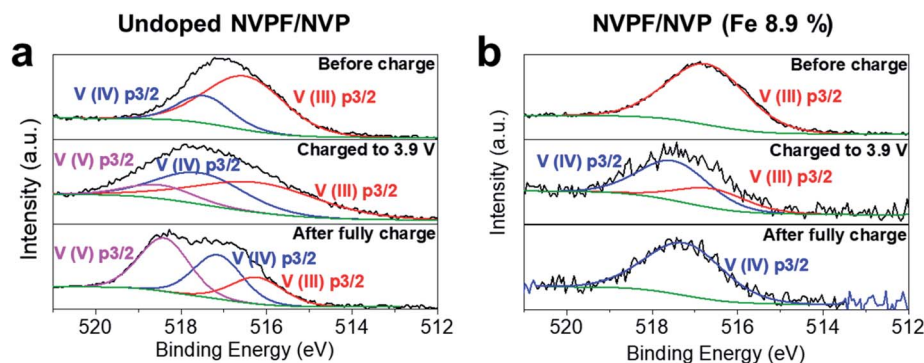

Fig. 4 Valence chance of V in NVPF/NVP (Fe 0%, 8.9%). V2p spectra of (a) undoped NVPF/NVP and (b) NVPF/NVP (Fe 8.9%). For undoped NVPF/NVP, V2p spectra are fitted with binding energies of 516.5 eV (V(III)) and 517.45 eV (V(IV)) before being charged; 516.24 eV (V(III)), 517.55 eV (V(IV)), and 518.5 eV (V(V)) after being charged to 3.9 V; 516.22 eV (V(III)), 517.14 eV (V(IV)), and 518.4 eV (V(V)) after being fully charged. For NVPF/NVP (Fe 8.9%), V2p spectra are fitted with the binding energies of 516.73 eV (V(III)) before being charged; 516.5 eV (V(III)) and 517.5 eV (V(IV)) after being charged to 3.9 V; and 517.25 eV (V(IV)) after being fully charged.
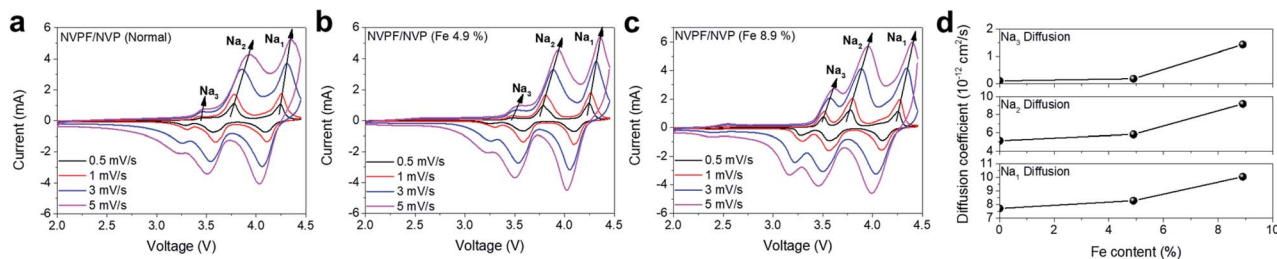
20440 | *J. Mater. Chem. A*, 2020, **8**, 20436–20445

This journal is © The Royal Society of Chemistry 2020

Fig. 5 Cyclic voltammetry analysis for NVPF/NVPs (Fe 0%, 4.9%, and 8.9%). Cyclic voltammetry profiles of (a, b and c) NVPF/NVP (Fe 0%, 4.9%, and 8.9%, respectively). (d) Na diffusivity variation at the three plateaus. Here, Na_1, Na_2, and Na_3 indicate current peaks corresponding to the first, second, and third plateaus.

sodium diffusivities in Fe-doped NVPF/NVPs (Fe 4.9% and 8.9%).

In order to measure the diffusion coefficients of NVPF/NVPs (Fe 0%, 4.9%, and 8.9%), cyclic voltammetry is utilized (Fig. 5a–c). The diffusion coefficients corresponding to the three main plateaus at ~4.2 V, ~3.7 V, and ~3.4 V are considered. The corresponding current peaks are labelled Na_1, Na_2, and Na_3, respectively. The linear relationship between i_p and $v^{1/2}$ allows employing the Randles–Sevcik equation to obtain the Na ion diffusion coefficients (Fig. 5d and S9†):

$$i_p = 2.686 \times n^{3/2} A D^{1/2} C v^{1/2}$$

Here, i_p, n, A, D, and v are the current peak, number of electrons during the reaction (here, $n = 2$), effective contact area (~1.54 cm²), Na ion diffusion coefficient, and voltage scan rate. For C, the concentration of Na^+ in the electrode, 0.0227 mol cm⁻³ for Na_1 and Na_2, and 0.0276 mol cm⁻³ for Na_3 is used on the basis of Na density in NVPF and NVP. As a result, indeed, NVPF/NVP

(Fe 8.9%) shows much improved Na ion diffusion coefficients at all three plateaus. Especially, the significant improvement of the Na ion diffusion coefficient in $Na_3V_{1.82}Fe_{0.18}(PO_4)_3$ at the third plateau would be due to the two-step variation with the buffer phase of $Na_{1+\alpha}V_{1.82}Fe_{0.18}(PO_4)_3$.

Another crucial kinetic property is the electronic conductivity. The electronic conductivity is closely related to the band gap of the material. Therefore, in order to examine the band gap change upon Fe substitution into NVPF, density functional theory (DFT) is conducted (Fig. 6). As a result, Fe substitution forms new energy levels below the existing conduction band. In consequence, the band gap of pristine NVPF at the Γ point substantially decreases from 2.193 eV to 1.464 eV upon 12.5% Fe substitution. The same trend in NVP was also reported.[28]

Fe substitution into NVPF/NVP evidently improves Na diffusivity and electronic conductivity. The improvements significantly affect operation at a higher current density. Unlike operation at low current density (i.e. 0.5C), NVPF/NVP (Fe 8.9%) presents
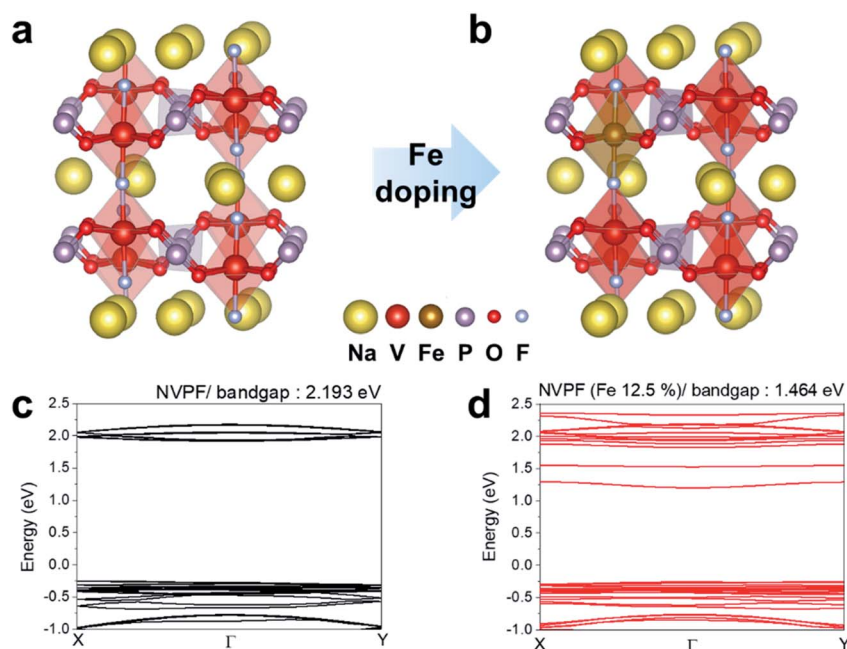

Fig. 6 DFT calculation on NVPF and Fe-doped NVPF. Atomic models showing the crystal structures of (a) $Na_3V_2(PO_4)_2F_3$ and (b) $Na_3V_{1.75}Fe_{0.25}(PO_4)_2F_3$. Band structures of (c) $Na_3V_2(PO_4)_2F_3$ and (d) $Na_3V_{1.75}Fe_{0.25}(PO_4)_2F_3$.

higher capacity contributions than NVPF/NVP (Fe 4.9%) from all three plateaus at a higher current density of 10C (Fig. S10†).

Perspective on practical applications

To realize an economically reasonable high performance SIB, the full cell configuration of the developed NVPF/NVP (Fe 8.9%) is examined in combination with bulk CuS, an attractive anode material with high theoretical capacity ($\sim$560 mA h g^{-1}), high conductivity ($\sim$10^3 S cm^{-1}),[7,29] and low cost. Furthermore, as we previously reported,[7] CuS exhibits a high practical capacity of $\sim$440 mA h g^{-1} at 1C and high capacity retention upon a long-term operation without any optimization in terms of size,

morphology, and surface coating. It is a huge advantage for commercialization. Despite the advantages of CuS, its application in full cells has not been reported yet.

The developed NVPF/NVP (Fe 8.9%)–CuS full cell is charged and discharged between 0 V and 4.25 V in the first cycle (Fig. 7a). After the first cycle, the voltage window is conservatively adjusted as 0 V to 4.05 V to prevent a capacity degradation caused by over charge. The full cell delivers a capacity of $\sim$101 mA h g^{-1} (based on the cathode material mass) and an energy density of $\sim$162.2 W h kg^{-1} (based on the mass of both electrode materials) with $\sim$2.09 V at 1C, which is close to the expected voltage level based on the practical average discharge voltage of

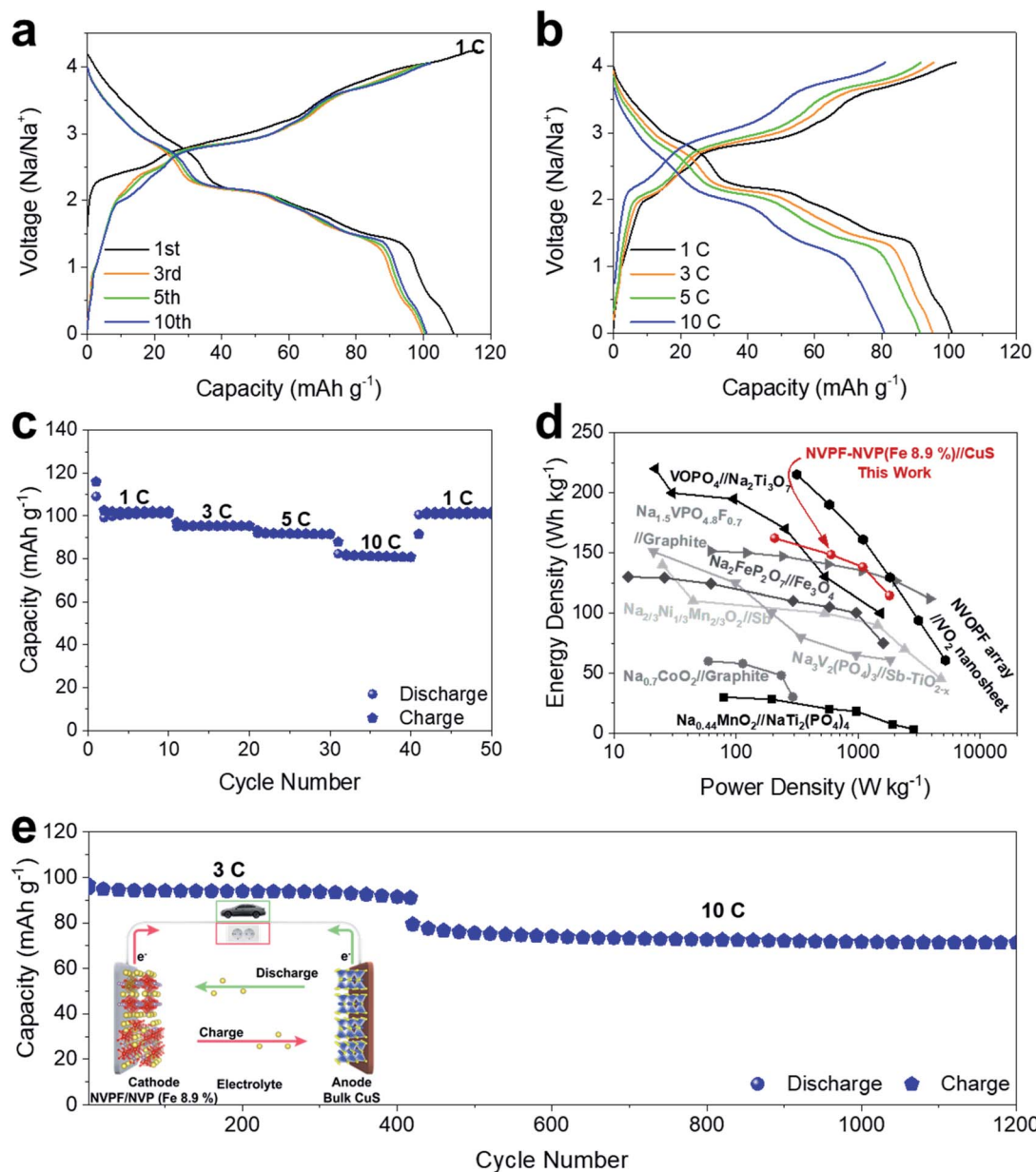
Fig. 7 Electrochemical performance of the NVPF/NVP (Fe 8.9%)–CuS full cell. Charge and discharge profiles of the full cell at the (a) 1st, 3rd, 5th, and 10th cycles at 1C, and (b) 1C, 3C, 5C, and 10C. (c) C-rate capability of the full cell from 1C to 10C. (d) The performance comparison with previously reported SIB full cells. (e) Cycling stability of the full cell at 3C and 10C, determined after the C-rate capability test in (c). The data points for the graph in (d) are extracted from recently reported studies[10,22] employing a tool in https://apps.automeris.io/wpd/.

20442 | J. Mater. Chem. A, 2020, **8**, 20436–20445

This journal is © The Royal Society of Chemistry 2020

Table 3 Full cell performance comparison between CuS//NVPF/NVP (Fe 8.9%) and recently reported SIB full cells. Average voltages are extracted using the tool in https://apps.automeris.io/wpd/

Anode and cathode combination	Energy density (W h kg^{-1} based on anode and cathode mass) @ C-rate (based on the cathode), and average voltage (V)	Capacity retention	Reference
VO$_2$ nanosheet//NVOPF nanocuboid array	215 W h kg^{-1} @ 1C, ~2.25 V	80 mA h g^{-1} @ 4C after 250 cycles (~80%), based on the cathode mass	22
NTO nanotube//VOPO$_4$	220 W h kg^{-1}, ~3.02 V	105 mA h g^{-1} @ 1C after 100 cycles (~92.3%), based on the cathode mass	31
Hard carbon//NVPF@rGO	161.61 W h kg^{-1} @ 0.5C, ~3.47 V	91 mA h g^{-1} @ 5C after 500 cycles (~75%), based on the cathode mass	21
Sb@TiO$_{2-x}$//NVP	151 W h kg^{-1} @ 5.16C, ~2.15 V	~350 mA h g^{-1} @ 0.66 A g^{-1} after 100 cycles (~63%), based on the anode mass	38
Graphite//Na$_{1.5}$VO$_{4.8}$F$_{0.7}$	~149 W h kg^{-1} @ 0.78C, ~3.1 V @ 100 mA h g^{-1} of 120 mA h g^{-1}	100.4 mA h g^{-1} @ 7.81C after 1000 cycles (~93%), based on the cathode mass	10
CuS//NVPF/NVP (Fe 8.9%)	**~162.2 W h kg^{-1} @ 1C, ~2.09 V**	**90 mA h g^{-1} @ 3C after ~450 cycles (~95%), based on the cathode mass, 71 mA h g^{-1} after ~450 cycles @ 3C and further 800 cycles @ 10C (~88%, based on the capacity @ 10C), based on the cathode mass**	**This work**

the NVPF/NVP (Fe 8.9%) composite (~3.67 V) and the average charge voltage of CuS (~1.55 V), respectively. The energy density of 162.2 W h kg^{-1} is ~79% of the theoretical value (Table S3†). Even at a high current density of 10C, it retains 81 mA h g^{-1} with an energy density of ~114.6 W h kg^{-1} (Fig. 7b–d). On the basis of its C-rate capability, the energy density is plotted as a function of the power density to compare the full cell with previously reported SIB full cells (Fig. 7d).[10,22,30–37] Despite its relatively low voltage, it ranks at a high position. It delivers energy densities of 148.59 W h kg^{-1}, 138.27 W h kg^{-1}, and 114.60 W h kg^{-1} at power densities of 599 W kg^{-1}, 1091.59 W kg^{-1}, and 1801.55 W kg^{-1}, respectively.

The NVPF/NVP (Fe 8.9%)–CuS full cell also exhibits high cycling stability (Fig. 7e). At a current density of 3C, it still retains ~91 mA h g^{-1} after ~450 cycles, which is ~95.7% of the initial capacity. Then, the current density is adjusted to 10C, and the cell is successively operated for ~800 cycles. Considering the initial capacity of 81 mA h g^{-1} at 10C, it still delivers ~87.6% of the capacity, 71.4 mA h g^{-1}, after 1200 cycles.

The suggested SIB full cell exhibits a well-balanced performance with the moderate energy density, superior cycling stability, and low raw material cost. In order to assess the competitiveness of the NVPF/NVP (Fe 8.9%)–CuS full cell, its performance is compared to those of previously reported SIB full cells[10,21,22,31,38] in terms of energy density, average voltage, cycling stability, and cost (Table 3 and Fig. S11†). Although it has a relatively low energy density compared to VO$_2$ nanosheet//NVOPF nanocuboid array and Na$_2$Ti$_3$O$_7$ (NTO) nanotube//VOPO$_4$ SIB full cells, it shows a superior capacity retention to them. In addition, it shows the lowest raw material cost among the candidates (Fig. S11 and Table S3†). Especially, the experimentally demonstrated performance is quite competitive to that of LTO-based LIBs, which are used in energy storage systems or high power applications, while its

cost is much less (Table S4†). Therefore, the suggested SIB full cell is quite suitable to support LIBs in energy storage systems and high power devices.

Conclusion

We do not only demonstrate that 8.9 atomic% Fe substitution into NVPF/NVP significantly enhances its sodium storage performance, but also conduct an in-depth study on the origin of the improved performance with *in situ* XRD, *ex situ* XPS, DFT calculation, and electrochemical characterization. Fe substitution into NVPF/NVP enables the complete utilization of the V^{3+}/V^{4+} redox pair in NVPF/NVP and two-step phase transition in NVP, which enhances the Na diffusivity. The reaction behavior of NVPF becomes close to biphasic rather than solid solution with Fe substitution. Furthermore, the band gap of the material is also reduced by Fe substitution to improve electronic conductivity. Finally, we materialize the previously suggested concept of the CuS–NVPF full cell by combining Fe-doped NVPF/NVP and CuS. On the basis of the earth abundances and low costs of Cu and S, the minimized V content in the NVPF/NVP composite, and the high energy density and long cycle life of CuS–NVPF/NVP (Fe 8.9%), we believe that it can be one of the most appealing candidates for energy storage systems and high power applications to support lithium ion batteries.

Author contribution

J. Y. P. and J. M. Y. designed the experiments. J. Y. P., H. J. L., Y. C., J. E. W., and D. K. K. synthesized cathode materials and performed electrochemical characterization. J. Y. P. and Y. C. conducted *in situ* XRD and analysis. Y. K. performed Rietveld refinement. J. Y. P., Y. L., and C. W. A. conducted *ex situ* XPS analysis. J. Y. P. and J. P. conducted EDS mapping in TEM. Y. S., K. Y., and C. W. L. performed DFT calculation for the band gap. J. Y. P. and co-authors prepared the manuscript under the supervision of J. M. Y.

This journal is © The Royal Society of Chemistry 2020

J. Mater. Chem. A, 2020, **8**, 20436–20445 | **20443**

Conflicts of interest

Acknowledgements

Notes and references

1 J. Qian, X. Wu, Y. Cao, X. Ai and H. Yang, High Capacity and Rate Capability of Amorphous Phosphorus for Sodium Ion Batteries, *Angew. Chem., Int. Ed.*, 2013, **52**, 4633–4636.

2 X. Dou, *et al.*, Hard carbons for sodium-ion batteries: structure, analysis, sustainability, and electrochemistry, *Mater. Today*, 2019, **23**, 87–104.

3 Z. Liu, *et al.*, Structure-designed synthesis of FeS_2@C yolk–shell nanoboxes as a high-performance anode for sodium-ion batteries, *Energy Environ. Sci.*, 2017, **10**, 1576–1580.

4 Y.-X. Wang, *et al.*, Uniform yolk-shell iron sulfide–carbon nanospheres for superior sodium–iron sulfide batteries, *Nat. Commun.*, 2015, **6**, 8689.

5 J. Huang, *et al.*, Nanostructures of solid electrolyte interphases and their consequences for microsized Sn anodes in sodium ion batteries, *Energy Environ. Sci.*, 2019, **12**, 1550–1557.

6 H. Kim, *et al.*, Sodium Storage Behavior in Natural Graphite using Ether-based Electrolyte Systems, *Adv. Funct. Mater.*, 2015, **25**, 534–541.

7 J. Y. Park, *et al.*, Pulverization-Tolerance and Capacity Recovery of Copper Sulfide for High-Performance Sodium Storage, *Adv. Sci.*, 2019, **6**, 1900264.

8 C. Wang, L. Wang, F. Li, F. Cheng and J. Chen, Bulk Bismuth as a High-Capacity and Ultralong Cycle-Life Anode for Sodium-Ion Batteries by Coupling with Glyme-Based Electrolytes, *Adv. Mater.*, 2017, **29**, 1702212.

9 B. Zhang, *et al.*, Microsized Sn as Advanced Anodes in Glyme-Based Electrolyte for Na-Ion Batteries, *Adv. Mater.*, 2016, **28**, 9824–9830.

10 Z.-L. Xu, *et al.*, Tailoring sodium intercalation in graphite for high energy and power sodium ion batteries, *Nat. Commun.*, 2019, **10**, 2598.

11 S. Yuvaraj, W. Oh and W.-S. Yoon, Recent Progress on Sodium Vanadium Fluorophosphates for High Voltage Sodium-Ion Battery Application, *J. Electrochem. Sci. Technol.*, 2019, **10**, 1–13.

12 X. Zhang, *et al.*, $Na_3V_2(PO_4)_3$: an advanced cathode for sodium-ion batteries, *Nanoscale*, 2019, **11**, 2556–2576.

13 Q. Liu, *et al.*, Carbon-coated $Na_3V_2(PO_4)_2F_3$ nanoparticles embedded in a mesoporous carbon matrix as a potential cathode material for sodium-ion batteries with superior rate capability and long-term cycle life, *J. Mater. Chem. A*, 2015, **3**, 21478–21485.

14 H. Yi, *et al.*, VSC-doping and VSU-doping of $Na_3V_{2-x}Ti_x(PO_4)_2F_3$ compounds for sodium ion battery cathodes: analysis of electrochemical performance and kinetic properties, *Nano Energy*, 2018, **47**, 340–352.

15 W. Liu, H. Yi, Q. Zheng, X. Li and H. Y. Zhang, Doped $Na_3V_2(PO_4)_2F_3$ compounds for sodium ion battery cathodes: electrochemical performance and analysis of kinetic properties, *J. Mater. Chem. A*, 2017, **5**, 10928–10935.

16 Y. Zhang, S. Guo and H. Xu, Synthesis of uniform hierarchical $Na_3V_{1.95}Mn_{0.05}(PO_4)_2F_3$@C hollow microspheres as a cathode material for sodium-ion batteries, *J. Mater. Chem. A*, 2018, **6**, 4525–4534.

17 Y. Makimura, L. S. Cahill, Y. Iriyama, G. R. Goward and L. F. Nazar, Layered Lithium Vanadium Fluorophosphate, $Li_5V(PO_4)_2F_2$: A 4 V Class Positive Electrode Material for Lithium-Ion Batteries, *Chem. Mater.*, 2008, **20**, 4240–4248.

18 T. Broux, *et al.*, Strong Impact of the Oxygen Content in $Na_3V_2(PO_4)$-$F_{3-y}O_y$ ($0 \leq y \leq 0.5$) on Its Structural and Electrochemical Properties, *Chem. Mater.*, 2016, **28**, 7683–7692.

19 R. Zhan, *et al.*, Half-cell and full-cell applications of sodium ion batteries based on carbon-coated $Na_3Fe_{0.5}V_{1.5}(PO_4)_3$ nanoparticles cathode, *Electrochim. Acta*, 2018, **283**, 1475–1481.

20 M. Peng, *et al.*, Hierarchical Ru-doped sodium vanadium fluorophosphates hollow microspheres as a cathode of enhanced superior rate capability and ultralong stability for sodium-ion batteries, *Nano Energy*, 2017, **31**, 64–73.

21 F. Li, *et al.*, Well-dispersed $Na_3V_2(PO_4)_2F_3$@rGO with improved kinetics for high-power sodium-ion batteries, *J. Mater. Chem. A*, 2020, **8**, 12391–12397.

22 D. Chao, *et al.*, Sodium Vanadium Fluorophosphates (NVOPF) Array Cathode Designed for High-Rate Full Sodium Ion Storage Device, *Adv. Energy Mater.*, 2018, **8**, 1800058.

23 Z. Mao, R. Wang, B. He, Y. Gong and H. Wang, Large-Area, Uniform, Aligned Arrays of $Na_3(VO)_2(PO_4)_2F$ on Carbon Nanofiber for Quasi-Solid-State Sodium-Ion Hybrid Capacitors, *Small*, 2019, **15**, 1902466.

24 L. Zhao, *et al.*, Delicate lattice modulation enables superior Na storage performance of $Na_3V_2(PO_4)_3$ as both an anode and cathode material for sodium-ion batteries:

20444 | *J. Mater. Chem. A*, 2020, **8**, 20436–20445

This journal is © The Royal Society of Chemistry 2020

understanding the role of calcium substitution for vanadium, *J. Mater. Chem. A*, 2019, **7**, 9807–9814.

25 M. Bianchini, *et al.*, Comprehensive Investigation of the $Na_3V_2(PO_4)_2F_3$–$NaV_2(PO_4)_2F_3$ System by Operando High Resolution Synchrotron X-ray Diffraction, *Chem. Mater.*, 2015, **27**, 3009–3020.

26 S. T. Dacek, W. D. Richards, D. A. Kitchaev and G. Ceder, Structure and Dynamics of Fluorophosphate Na-Ion Battery Cathodes, *Chem. Mater.*, 2016, **28**, 5450–5460.

27 M. Bianchini, P. Xiao, Y. Wang and G. Ceder, Additional Sodium Insertion into Polyanionic Cathodes for Higher-Energy Na-Ion Batteries, *Adv. Energy Mater.*, 2017, **7**, 1700514.

28 X. Liu, *et al.*, Insight into Preparation of Fe-Doped $Na_3V_2(PO_4)_3$@C from Aspects of Particle Morphology Design, Crystal Structure Modulation, and Carbon Graphitization Regulation, *ACS Appl. Mater. Interfaces*, 2019, **11**, 12421–12430.

29 J. Y. Park, *et al.*, Atomic visualization of a non-equilibrium sodiation pathway in copper sulfide, *Nat. Commun.*, 2018, **9**, 922.

30 I. Hasa, *et al.*, A sodium-ion battery exploiting layered oxide cathode, graphite anode and glyme-based electrolyte, *J. Power Sources*, 2016, **310**, 26–31.

31 H. Li, *et al.*, An advanced high-energy sodium ion full battery based on nanostructured $Na_2Ti_3O_7$/$VOPO_4$ layered materials, *Energy Environ. Sci.*, 2016, **9**, 3399–3405.

32 S. Guo, *et al.*, A High-Voltage and Ultralong-Life Sodium Full Cell for Stationary Energy Storage, *Angew. Chem., Int. Ed.*, 2015, **54**, 11701–11705.

33 L. Liang, *et al.*, Large-scale highly ordered Sb nanorod array anodes with high capacity and rate capability for sodium-ion batteries, *Energy Environ. Sci.*, 2015, **8**, 2954–2962.

34 H. Xiong, M. D. Slater, M. Balasubramanian, C. S. Johnson and T. Rajh, Amorphous TiO_2 Nanotube Anode for Rechargeable Sodium Ion Batteries, *J. Phys. Chem. Lett.*, 2011, **2**, 2560–2565.

35 Y. Wang, R. Xiao, Y.-S. Hu, M. Avdeev and L. Chen, P2-$Na_{0.6}[Cr_{0.6}Ti_{0.4}]O_2$ cation-disordered electrode for high-rate symmetric rechargeable sodium-ion batteries, *Nat. Commun.*, 2015, **6**, 6954.

36 Z. Li, D. Young, K. Xiang, W. C. Carter and Y.-M. Chiang, Towards High Power High Energy Aqueous Sodium-Ion Batteries: The $NaTi_2(PO_4)_3$/$Na_{0.44}MnO_2$ System, *Adv. Energy Mater.*, 2013, **3**, 290–294.

37 L. Wang, *et al.*, Rhombohedral Prussian White as Cathode for Rechargeable Sodium-Ion Batteries, *J. Am. Chem. Soc.*, 2015, **137**, 2548–2554.

38 N. Wang, Z. Bai, Y. Qian and J. Yang, Double-Walled $Sb@TiO_{2-x}$ Nanotubes as a Superior High-Rate and Ultralong-Lifespan Anode Material for Na-Ion and Li-Ion Batteries, *Adv. Mater.*, 2016, **28**, 4126–4133.

This journal is © The Royal Society of Chemistry 2020

J. Mater. Chem. A, 2020, **8**, 20436–20445 | **20445**